Ultramicroscopy 200 (2019) 139–148

Contents lists available at ScienceDirect

Ultramicroscopy

journal homepage: www.elsevier.com/locate/ultramic

Insights into image contrast from dislocations in ADF-STEM

E. Oveisi[a,b,*], M.C. Spadaro[a], E. Rotunno[c], V. Grillo[c,d], C. Hébert[a,b,*]

[a] Interdisciplinary Centre for Electron Microscopy, École Polytechnique Fédérale de Lausanne (CIME-EPFL), Lausanne, Switzerland
[b] Electron Spectrometry and Microscopy Laboratory, École Polytechnique Fédérale de Lausanne (LSME-EPFL), Lausanne, Switzerland
[c] Institute of Nanoscience, National Research Council (NANO-CNR), Modena, Italy
[d] Institute of Materials for Electronics and Magnetism, National Research Council (IMEM-CNR), Parma, Italy

ARTICLE INFO

Keywords:
ADF-STEM
Dislocation contrast
Electron channelling
Bloch-wave scattering theory
Grillo's strain-channelling equation

ABSTRACT

Competitive mechanisms contribute to image contrast from dislocations in annular dark-field scanning transmission electron microscopy (ADF-STEM). A clear theoretical understanding of the mechanisms underlying the ADF-STEM contrast is therefore essential for correct interpretation of dislocation images. This paper reports on a systematic study of the ADF-STEM contrast from dislocations in a GaN specimen, both experimentally and computationally. Systematic experimental ADF-STEM images of the edge-character dislocations reveal a number of characteristic contrast features that are shown to depend on both the angular detection range and specific position of the dislocation in the sample. A theoretical model based on electron channelling and Bloch-wave scattering theories, supported by numerical simulations based on Grillo's strain-channelling equation, is proposed to elucidate the physical origin of such complex contrast phenomena.

1. Introduction

Defect analysis in crystalline materials provides important insights into many properties of materials across a broad range of applications [1]. While conventional transmission electron microscopy (CTEM) has commonly been used to advancing the field of crystalline defect analysis, recently interest has emerged in using scanning TEM (STEM) to elucidate defect structure. STEM is particularly appropriate for studying much thicker samples than CTEM normally allows, as well as for obtaining images suitable for stereoscopic or tomographic reconstructions in which dynamical contrast effects are reduced [2-9]. Such interesting characteristics of the STEM images arise because the scattered state wave vectors are integrated over the acceptance range of an annular detector [10]. By using different detectors at the same time, various imaging modes, for instance bright-field (BF) and annular dark-field (ADF), are simultaneously accessible [11]. Depending on the detector geometry and beam convergence angle, there are several independent mechanisms contributing to defect contrast in the STEM images, making image interpretation complex [12,13].

Since the first demonstrations of using STEM for defect analysis in the 1970s, many mechanisms have been proposed to treat the ADF-STEM images [10,12,14-18]. Maher and Joy were the first to apply the principle of reciprocity for defect image interpretation by using fixed-beam dynamical theory of electron diffraction [15]. They showed that the geometry of crystalline defects could be assessed by STEM diffraction analysis methods as is done in CTEM. Electron diffraction contrast has been used in many other studies to interpret defect image contrast [4,19,20]. Perovic et al. used Bloch-wave scattering theory as an alternative approach to elucidate the effect of elastic strain on the contrast of the ADF images [10,18]. According to their theory, the contrast is associated with the Bloch-wave interference effects through the foil thickness, and therefore depends on the specific position of the defect in the foil. In the Bloch-wave theory of defect analysis, the presence of strain field affects the excitation of the Bloch-waves, resulting in interband transitions between the Bloch-wave states. The Bloch-wave theory has also been applied to analyse the contrast around the defects at the atomic scale [21].

A closely related approach for interpreting dislocation image contrast, known as de-channelling, was suggested by Cowley and Huang [14]. In the electron channelling process, the atomic sites act as nanolenses concentrating the beam along the attractive potential of the column, which in the Bloch-wave model is considered as strong excitation of the localized *1s*-type waves [22-25]. The non-dispersive *1s*-type Bloch-states that are localized on the atomic sites dominate the signal at high scattering angles [22,23,26]. In the de-channelling theory, image contrast results from any disruption of the channelling process. Distortion of the lattice channels by the strain field close to a crystal defect or, on a broader scale, loss of the wave-field symmetry

* Corresponding authors.
E-mail addresses: emad.oveisi@epfl.ch (E. Oveisi), cecile.hebert@epfl.ch (C. Hébert).

https://doi.org/10.1016/j.ultramic.2019.02.004
Received 1 August 2018; Received in revised form 2 January 2019; Accepted 6 February 2019
Available online 12 February 2019

close to the crystal surface interrupt the channelling condition, thus can be considered as an origin for signal in the ADF images [14].

Grillo et al. studied the effect of long-range strain and local static displacements on the forward propagation of the wave function [17]. They proposed that in case of large static displacements the curvature of atomic planes should be taken into account instead of atomic displacements [17]. Where atomic column inclination happens, the wave states on either side of the crystal need to be matched, causing in turn an additional diffuse scattering. Local lattice distortion or atomic displacements at dislocation cores also generates static diffuse scattering that, by analogy to X-Ray scattering process, is called Huang scattering [27-30]. Huang scattering analogous with the thermal diffuse scattering (TDS) has the effect of weakening the Bragg reflections; but, contrary to the TDS is time independent and contains little information about the atomic number [30]. Grillo et al. described the scattering angle dependence of the ADF strain contrast as a result of the contribution of two competitive mechanisms: Huang scattering and de-channelling [17]. Simulations demonstrated that strain fields reduce the propagation of the forward wave function, thus has a similar contribution to a wide range of scattering angles, from low to high angles [31]. On the other hand, the intensity of the scattering due to static displacements is angle-dependent, and decreases rapidly as the angle is increased. While at low angles the contrast of static displacements is determined by Huang scattering and de-channelling events, which act inversely, at higher angles the contribution of Huang scattering becomes less important, and therefore contrast from strained regions decreases as it is dominated by the de-channelling process [31].

Overall, due to the complexity of the mechanisms contributing to contrast from defects in ADF-STEM images, it is often essential to couple image simulations with experimental data for a correct interpretation of defect contrast [16,19,20]. Here, we use Bloch-wave scattering and electron channelling theories to further report on the ADF-STEM dislocation contrast mechanisms. We apply this approach to interpret the contrast features that ascertained to depend on both ADF detection range and specific position of the defect in the sample. We couple the experimental images with simulations that have been carried out using an improved version of Grillo's strain-channelling equation system to further explore the depth-dependent ADF dislocation contrast [32, 33].

2. Experimental and computational procedures

2.1. Specimen

For this study, a thin film of gallium nitride (GaN) with relatively high content (about 10^{10} cm^2) of edge- and mixed-character dislocations was used (details on GaN growth in [34]). To prepare sample for STEM analysis, a cross-sectional lamella was extracted along the growth direction of the GaN membrane (i.e. parallel to its (1 $\bar{1}$ 0 0) crystallographic plane). This process was done through conventional focused ion beam (FIB) lift-out in a Zeiss NVision40. The thinning process was followed by low energy final polishing with the FIB (2 kV and 60 pA) to minimize the ion-induced damage and to obtain a foil with a uniform thickness of about 200 nm. During the preparation process the site of interest had been covered with a protective layer through FIB-assisted carbon deposition.

2.2. Electron microscopy

To investigate the angular dependence of ADF image contrast from dislocations of different depths, a systematic experiment varying the annular detector collection range was performed in a FEI Tecnai-Osiris at 200 kV. The contrast was studied for threading edge-character dislocations that were located close to entrant and exit foil surfaces while the specimen was tilted to satisfy a [1 $\bar{1}$ 0 0] zone axis orientation. Burgers vectors of the threading dislocations in the GaN membrane were determined using the invisibility criterion (i.e. **g.b** analysis) under $\mathbf{g} = (0\ 0\ 0\ 2)$ and $\mathbf{g} = (1\ 1\ \bar{2}\ 0)$ diffraction conditions (Figure S1, Supplementary materials). The approximate depth of dislocations in the GaN foil was determined using thickness fringes (see Figure S2, Supplementary materials) [35].

Table 1
ADF-STEM detector collection angles (mrad) as a function of camera length (mm)[a].

	Detector collection angle (mrad)	
	β_{in}	β_{out}
Camera length		
34	180	200
43	175	200
54	139	200
75	100	200
87	86.4	200
115	65.3	200
165	45.5	200
220	34.2	200
330	22.8	139
550	13.7	83.6
770	9.7	59.7

[a] The upper limit of 200 mrad is due to the cut-off by the pole-pieces and

Series of STEM images were acquired with an ADF detector over a range of camera lengths (between 34 mm and 770 mm). Table 1 lists the collection range of the detector as a function of camera length. The images were acquired at two magnifications: low magnification, (2.4 nm pixel size, 48 msec dwell time); high magnification, (0.3 nm pixel size, 6 msec dwell time). At each camera length the detector gain and amplitude (brightness and contrast) were adjusted to increase the visibility of the image features. During the experiments, the illumination convergence semi-angle of the incident probe was set to 9.7 mrad, using a nominal 50 µm condenser aperture. Energy-filtered convergent beam electron diffraction (CBED) patterns were acquired on a JEOL-2200FS operated at 200 kV in nano-beam mode and zero-loss filtered with an energy slit of 30 eV.

2.3. Numerical simulations

Grillo's strain-channelling equation was implemented for the simulations of the ADF dislocation contrast. Grillo's strain-channelling equation starts from the Bloch-wave scattering theory and explicitly describes the evolution of the highly excited *1s*-type states after interaction with the sample [33, 36]. In order to introduce and account for all sample features the equation contains several parameters; some depend on the sample and strain features (thickness, defect depth, strain-related atomic column curvature, etc.), and others govern the contrast in different detection regimes. Here, we use a modified version of this code that more specifically describes the contribution of Huang scattering to image formation, in particular the scattering produced at middle angle range by the higher energy non-*1s* Bloch-states. These modifications are described in detail in the appendix. The defect core size was set to 25 Å and simulations were carried out for straight defects at different depths (from 20 to 180 nm) in a 200 nm thick GaN sample. Surface relaxation was included during simulations. The material absorption coefficient and the curvature of the atomic column were fixed to 5×10^{-3} $Å^{-1}$ and 3×10^{-4} $Å^{-1}$, respectively. The source code is written in C^{++} and has been implemented in the STEM_CELL software [33, 36].

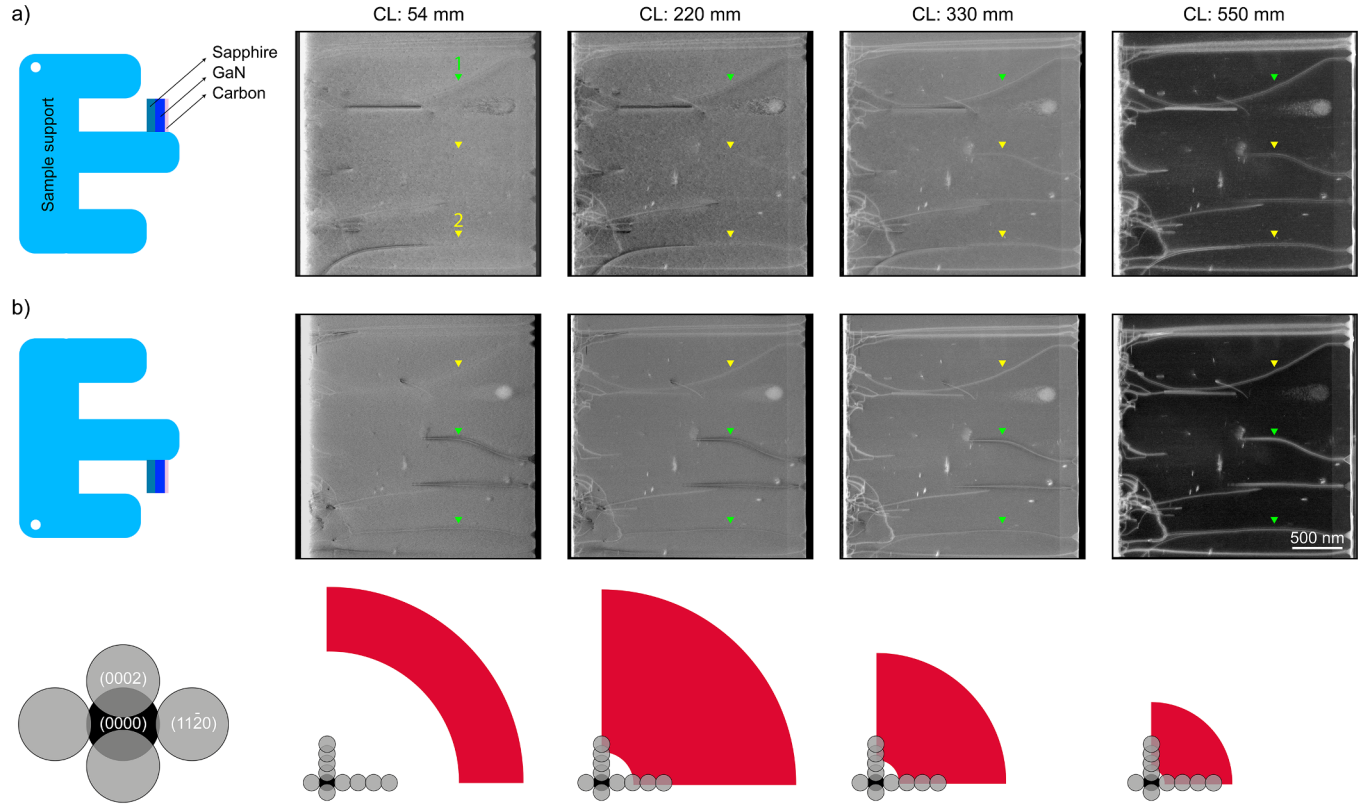

Fig. 1. A comparison between dislocation contrasts over a range of ADF detection angles. (a) Changes in the contrast from dislocations of different specific depths in the GaN sample with varying the ADF detection range. Arrows encode the approximate position of dislocation in the specimen: green, dislocation close to entrant foil surface; yellow, dislocation close to exit foil surface. The GaN sample is orientated to have the [1 $\bar{1}$ 0 0] direction parallel with the electron beam. (b) ADF-STEM images of the same region of the sample after flipping the specimen upside down in the microscope. To ease the comparison, the bottom row images (b) are flipped horizontally. To the bottom of each column, a schematic of the ADF detector and zone axis STEM diffraction configuration are shown. Schematics on the left side of each row demonstrate the geometry of the specimen in the microscope. (For interpretation of the references to colour in this figure legend, the reader is referred to the web version of this article.)

3. Results and discussions

3.1. Experimental results

The angular collection range β of an ADF detector ranges from low-angle at large camera lengths to medium-angle, and finally to high-angle when further decreasing the camera length. Based on the angular collection range of the detector, we classify the ADF images into three regimes: low-angle ADF (LAADF), $20 < \beta < 60$ mrad; medium-angle ADF (MAADF), $40 < \beta < 120$ mrad; and high-angle ADF (HAADF), $\beta_{in} > 80$ mrad. In the LAADF regime, both elastic Bragg and diffuse scattering significantly contribute to image signal. The contribution of Bragg scattering decreases in the MAADF regime, and in the HAADF regime is overtaken by TDS and Rutherford scattering.

A series of representative ADF-STEM images showing the sample in different regimes is given in Fig. 1. Different image contrasts are observed for the top- and bottom-configuration dislocations (i.e. close to entrant and exit foil surface, respectively) in different regimes, revealing that the ADF dislocation contrast depends sensitively on the specific position of a dislocation in the foil. The bottom-configuration dislocations gradually lose their visibility as the detector collection range is increased to MAADF regime, and are finally just barely visible in the HAADF regime. On the contrary, the top-configuration dislocations remain visible in all the three regimes. Further investigations indicated that the contrast features vary for different regimes. To better visualize the evolution of dislocation contrast as a function of angular collection range, series of images from two dislocations that are located close to the entrant and exit foil surfaces (marked 1 and 2 in Fig. 1, respectively) are presented in Fig. 2. The intensity profiles across these two dislocations are plotted in Fig. 3, highlighting a contrast reversal for the top-configuration dislocations between the LAADF and HAADF regimes (see also the region marked by red rectangles in Fig. 2). The bottom-configuration dislocations do not show this contrast reversal, but gradually lose their visibility towards the HAADF regime as the detector angular range is increased. To verify the reproducibility of such depth-dependent contrast mechanism, the aforementioned dislocations are imaged after flipping the specimen in the microscope. This is demonstrated in Fig. 2c,d, confirming the existence of a similar trend. It should be noted that a similar trend has also been observed in the images that were simultaneously acquired with another ADF detector ("DF4") that has a smaller inner/outer diameter [37].

To further study the contrast reversal mechanism that happens for the top-configuration dislocations, images at higher magnifications are acquired. The images highlight that the contrast features from a top-configuration dislocation change entirely when acquired in different regimes. In the LAADF regime the contrast is composed of a narrow line (FWHM $\approx$ 4 nm) of negative contrast (i.e. with lower intensities relative to the background), surrounded by two parallel lines of positive contrast on either side of the dislocation line. On each side of the dislocation line, the width of the region with positive contrast is about 7 nm. As of now in the text this contrast feature will be referred to as *M-type* contrast. As demonstrated in Figs. 2 and 3b, the *M-type* contrast

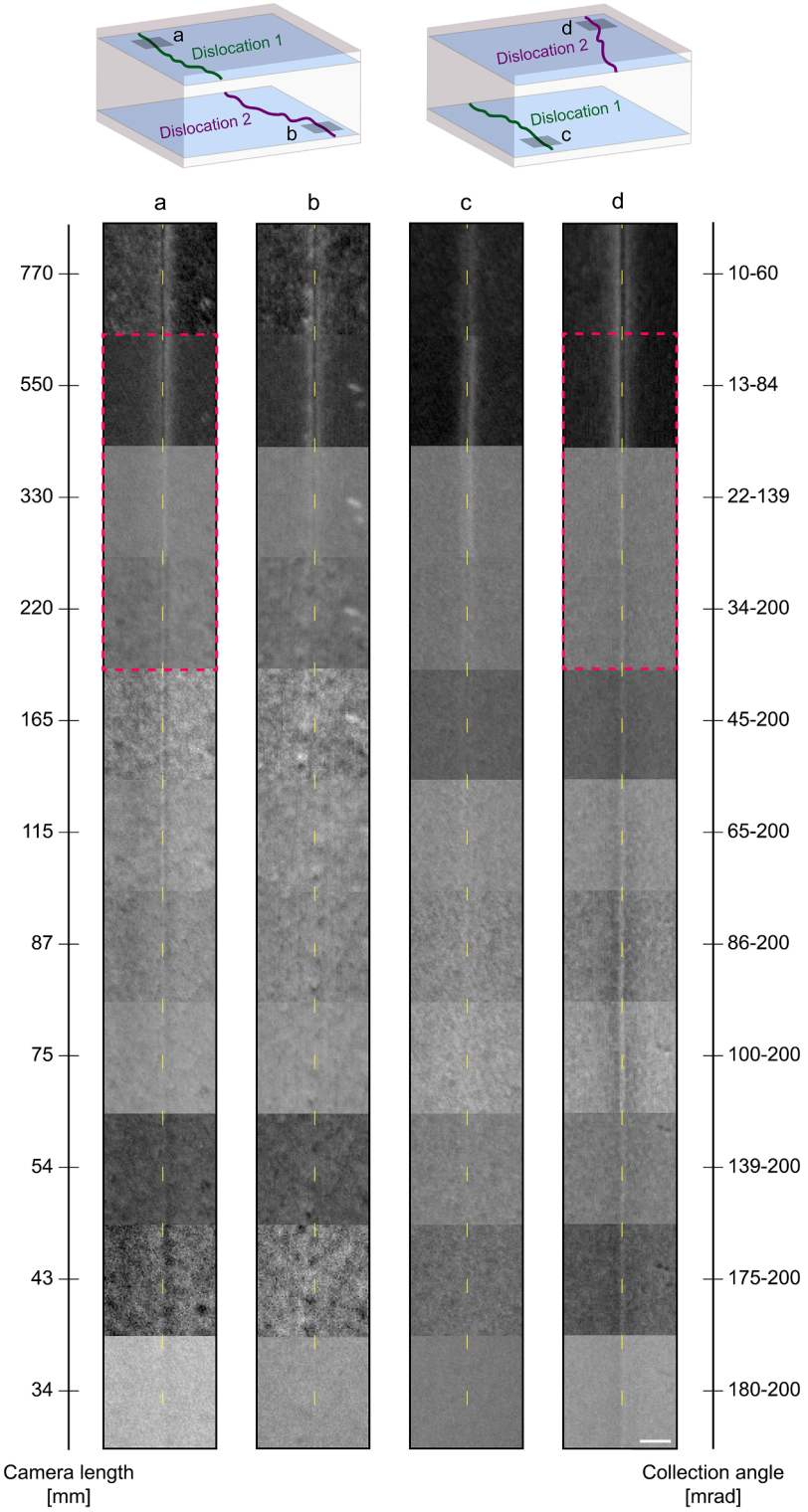

Fig. 2. Illustration of dislocation image contrast evolution with varying ADF detection range. (a,b) Dislocations 1 and 2 of Fig. 1, respectively. Images of the same dislocations after flipping the specimen upside down in the microscope are shown in (c, close to exit foil surface) and (d, close to entrant foil surface). The change in contrast is different for the top- and bottom-configuration dislocations. The contrast is adjusted to increase the visibility of the image features. Scale bar is 50 nm.

characteristic of the LAADF regime appears to be independent from dislocation depth in the foil and is identical for the top- and bottom-configuration dislocations. The contrast of the top-configuration dislocations changes from *M-type* to a sharp single peak, so-called *I-type*, when acquired in the MAADF regime. This sharp peak remains visible for larger collection ranges. Finally, in the HAADF regime, the top-configuration dislocations exhibit a so-called *W-type* contrast; a contrast that is complementary to the *M-type* contrast characteristic of the LAADF regime. Examples of the *M-*, *I-*, and *W-type* contrasts are illustrated in Fig. 4.

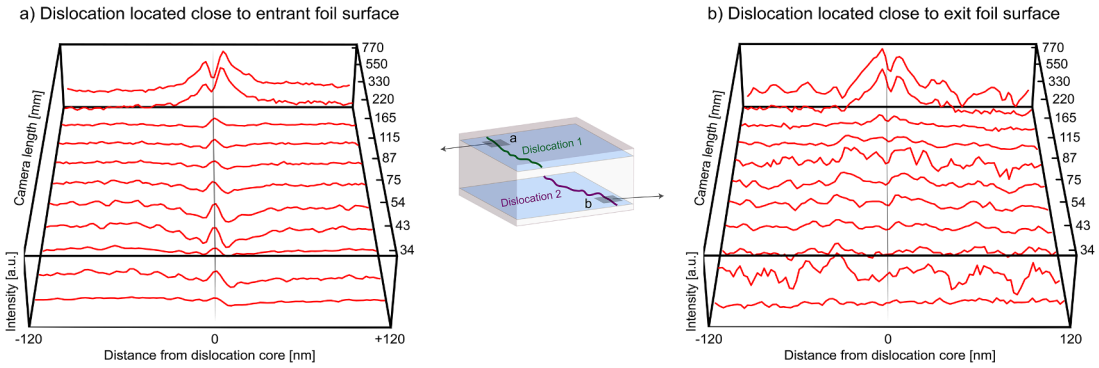

Fig. 3. Line scans of intensity profile across dislocations of Figs. 2a and 2b. (a) Dislocation 1, located close to entrant foil surface; (b) Dislocation 2, located close to exit foil surface. The transparent grey plane on the plots indicates the approximate position of the dislocation core. The intensity profiles are 240 nm long and the intensity is integrated over a region of 60 nm wide. Spatial drift between the images of the stack was corrected using the method described in [38].

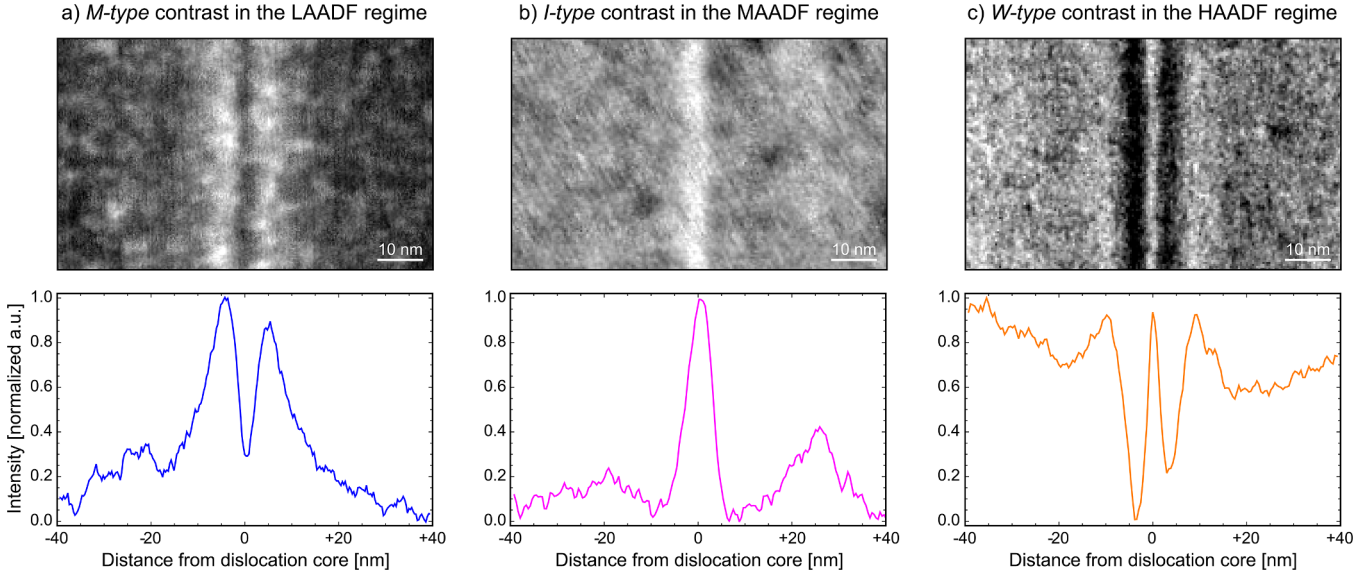

Fig. 4. Experimental image contrasts from a top-configuration dislocation acquired in different ADF-STEM regimes: (a) LAADF regime, *M-type* contrast; (b), MAADF regime, *I-type* contrast; (c) HAADF regime, *W-type* contrast. Bottom images: corresponding intensity line profiles. The intensity profiles are integrated over 150 pixels.

The *M-type* contrast in the LAADF regime is directly interpretable using the classical Bragg diffraction theory [39]. Considering the significant contribution of the low-order elastic Bragg reflections to the LAADF signal, the appearance of the *M-type* contrast can be attributed to the changes in diffraction condition from the strained regions around the dislocation core; local variations of the deviation parameter (s_g) in the strained regions result in a positive contrast on either side of the dislocation core. Due to contributions of multiple diffracted beams with a range of deviation parameters, the region exhibiting positive contrast is wide ($\approx$ 7 nm). The non-uniform intensity on either side of dislocation core is probably due to slight deviation from the exact zone axis condition.

De-channelling of the electron probe in the presence of strain has also been proposed as a source of enhanced signal in the LAADF regime [14]. In the de-channelling theory, changes in the electron wave vector due to the dislocation strain field produce an expansion of the diffraction pattern. This is consistent with experimental observations in Fig. 5, where we compare the CBED patterns from different regions across a dislocation line. The CBED pattern spreads out when the beam crosses the strained regions around the dislocation core, and the direction of this expansion is opposite on both sides of the dislocation core. Therefore, it can be assumed that the origin of the intensity increase on either side of the dislocation core is due the overlap between the expanded region of the CBED pattern and the annular detector. This also explains how such an enhanced signal can disappear when the inner collection angle of the detector is larger than $\approx$ 40 mrad, e.g. for CL $\leq$ 330 mm, in the MAADF regime. However, interestingly no expansion is observed in the CBED pattern of the dislocation core, which rather resembles those of regions far away from the dislocation strain field. This justifies why there is no gain in the LAADF signal from dislocation core, a region that accommodates the greatest atomic displacements. This latter phenomenon can be explained by taking into account that long-range strain and local static displacements affect the forward propagation of the wave function differently [17]. As proposed by Grillo et al., in case of large static displacements, i.e. regions around dislocation core, curvature of atomic planes should be taken into account as a source for the ADF signal [16]. Accordingly, the enhanced LAADF signal on either side of dislocation core stems from the diffuse scattering (Huang scattering) that arises from the large lattice curvature in the strained regions around a dislocation core. In contrast, a trajectory passing through the core of an edge-character dislocation encounters a curvature field close to zero, thus no signal modification is expected from the dislocation core region; with the exception of a peculiarity at higher collection angles due to a minimal effect on the electron beam

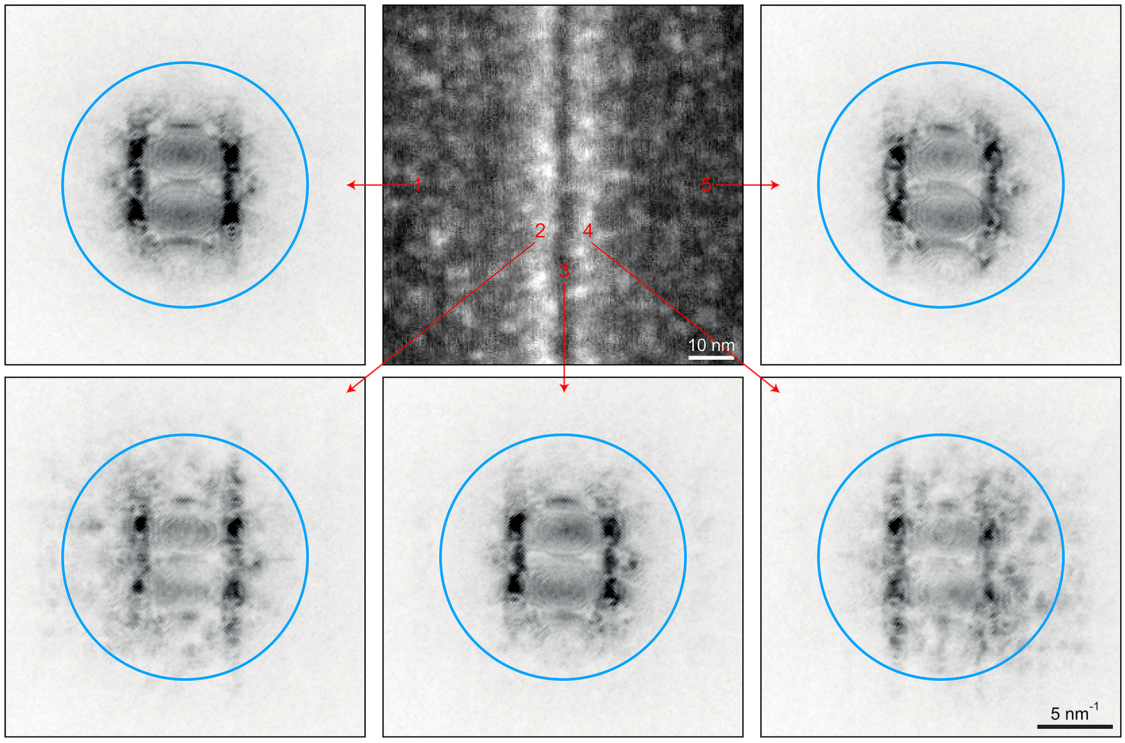

Fig. 5. Illustration of the energy-filtered CBED patterns from different regions around an edge-character dislocation. Expansion of the CBED pattern is obvious for the adjacent regions either side of the dislocation core (regions 2 and 4). Relative to the intact regions (marked 1 and 5), the extent of the expansion of the CBED pattern is about 30 mrad, explaining the appearance of the *M-type* contrast in the LAADF regime only. The blue circle indicates the location of the annular detector of 20 mrad inner collection angle. (For interpretation of the references to colour in this figure legend, the reader is referred to the web version of this article.)

propagation that will be discussed later.

Huang scattering, which is produced by the bending of atomic columns, contributes mainly to the LAADF signal due to the slowly changing displacements. Conversely, a very abrupt lateral displacement of the atoms occurs in the proximity of the dislocation core and its effects can be assimilated to the most disordered motions: thermal vibration. According to the classic simple model used by Yu et al. [40], scattering due to the presence of the extreme strain field at the dislocation core can be treated as the one related to the thermal diffuse scattering, therefore covering a larger angular range. This means there exists a regime from MAADF to moderate HAADF where this second type of diffuse scattering (so-called extra Huang scattering) produces a positive contribution to the intensity for generating the *I-* and *W-type* contrasts.

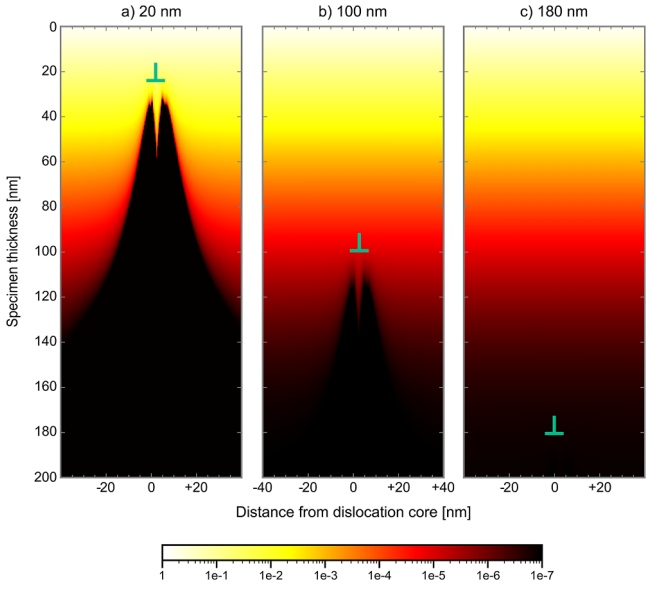

Fig. 6. Propagation of the *1s* Bloch-state as a function of sample thickness and evaluated for different dislocation depths. The dislocation is located (a) 20 nm below the entrant surface, (b) in the middle of the sample and (c) 20 nm above the exit surface. The colour of each pixel encodes the intensity (*1s* state amplitude) in logarithmic scale.

The Bloch-wave scattering theory can be used to further interpret the contrast features introduced above. To illustrate this concept in Fig. 6 we report the intensity of the *1s* state wave in a cross section of the foil, normal to the dislocation line and evaluated for different dislocation depths using Grillo's strain equation. Since the crystal is oriented in a strong axial channelling condition (i.e. zone axis), electrons are well channelled before encountering the dislocation. Therefore the intensity of the *1s* state at the entrant foil surface is set to unity. As the electron beam propagates through the sample, the intensity rapidly decreases due to absorption and completely vanishes before reaching the opposite surface of the specimen. The presence of defects drastically changes the beam propagation since the *1s* state is de-channelled into other Bloch-states, which is due to the curvature of atomic planes around the dislocation core (Fig. 6a and 6b). The rate at which the *1s* state is de-channelled depends on the magnitude of the curvature; close to the dislocation core the *1s* state is almost immediately de-channelled into other Bloch-states and its intensity drops to zero, while further away it can propagate longer in the sample. The innermost region of the dislocation core is an exception, as is discussed in more detail in the next section. Note that a dislocation located close to the bottom surface of the specimen (Fig. 6c) has no influence on the propagation of the *1s* state because all its intensity has already been de-channelled.

Changes in the excitation of the *1s* state is linked directly to the generation of diffuse scattering, which represents the main mechanism generating a signal at medium to high scattering angles (MAADF and

HAADF regimes). The *W-type* contrast observed in the HAADF regime thus reflects different propagation distances of the *1s* state inside the foil as a function of the distance from the dislocation core. The differences in the scattering angle of the excited Bloch-states also has to be considered for the interpretation of the contrast. The scattering angle of the diffusely de-channelled electrons is not the same for all Bloch-states, being larger for the *s*-type states compared to the others. The *s*-type states propagate very close to atomic sites and thus, contrary to the other states that are mainly concentrated between the atoms, will experience diffuse scattering to higher angles. Therefore, it can be assumed that the scattering angle of the electrons being diffused from the dislocation core is greater than those generated due to the strain around it. They can therefore be made visible only by increasing the inner collection angle of the detector (i) to the MAADF regime, in which the *I-type* contrast is detected, and (ii) to the HAADF regime, where it sums with the intensity already present in the dislocation position. In fact, the strained regions at both sides of the dislocation core affect the excitation of higher Bloch-states, generating diffuse scattering mainly in the LAADF regime. Therefore at large inner collection angles, in the HAADF regime, these regions appear with a negative contrast compared to the regions far away from the strain field. As a result, contrast of a top-configuration dislocation in the HAADF regime is complementary to that in the LAADF regime, i.e. the *W-type* and *M-type* contrasts, respectively. Further increase of the outer collection angle increases the contribution from dynamic TDS to the image signal, resulting in overshadowing of the diffusely scattered signal from static atomic displacements, thus reduces the visibility of defects.

In summary, the depth-dependent contrast behaviour can be described by diffuse scattering based on the Bloch-wave channelling model and is regarded to be due to the attenuation of the *1s* Bloch-state in the specimen thickness (Fig. 6c). Channelling related effects that give rise to dislocation contrast at medium to high angles are less important in the bottom of a thick specimen, where the *1s* state is completely absorbed. Hence dislocations located at the bottom segment should appear with a faint contrast in the MAADF and HAADF regimes. On the other hand, the enhanced signal in the *M-type* contrast of the LAADF regime is caused by the scattering of any Bloch-state, and not only the *1s* state. Since high-energy states remain populated even at the bottom of the foil, the LAADF signal is less sensitive to the position of the dislocation in the foil. Conversely, the *I-type* and *W-type* contrasts that are dominated by scattering of the *1s* Bloch-state fade away for the bottom-configuration dislocations in the MAADF and HAADF regimes.

3.2. Computational results

To computationally validate our proposed theory, numerical simulations are performed based on Grillo's equation. Taking into account all the factors that influence electron beam propagation inside the sample, the ADF dislocation contrast is computed for three different angular regimes (i.e. LAADF, MAADF, and HAADF).

As expected, depending on the strain amplitude, the atomic columns around the dislocation core are distorted differently. In Fig. 7 we show a series of multislice simulations of the propagation of the electron beam along a curved atomic column. The sample represents a single Ga column in a 15 nm thick GaN foil with the [1 $\bar{1}$ 0 0] direction oriented along the electron beam direction. The electron beam propagation is simulated for different curvature radii. For small curvature radii the electron beam is able to follow the curved column (Figs. 7a-7d). As a result of the curvature the beam is rapidly de-channelled as testified by the rapidly decreasing intensity and the disappearing of the *Pendellösung* oscillations. However, when the curvature exceeds a critical value (Fig. 7e), the electron channelling is completely disrupted and the beam propagates as it does in an amorphous material. In order to account for the effect of large atomic column curvatures, we introduce the reduced curvature Γ' defined as:

$$\Gamma' = \begin{cases} \frac{2m}{\pi}\sin\left(\frac{\pi\Gamma}{2m}\right), & if\ |\Gamma| < 2m \\ 0, & otherwise \end{cases}$$

where m is the maximum curvature value of the atomic column for which the primary electron beam is able to be channelled, and Γ is the real column curvature. It can be noted that for small values of the curvature Γ and Γ' coincide while Γ' progressively approaches 0 as the curvature increases. This definition of the reduced curvature reflects the fact that only a fraction of the beam is channelled along the curved atomic column while the remaining part will freely propagate in the specimen and contribute to the Huang scattering.

This approach was also tacitly used in the previous version of Grillo's equation [16], but is made more explicit herein. Accordingly, a HAADF signal similar to that of the unstrained matrix is expected at the dislocation core. However, as can be seen in the experimental images, at the dislocation core, where Γ' is supposed to be 0, the intensity is higher than in the matrix. The MAADF intensity at the core location also shows a similar behaviour. To explain this phenomenon we go into more detail regarding the Huang scattering main features. As explained earlier, we are facing a second type of diffuse scattering (i.e. extra Huang scattering) that is qualitatively different from the one described in the previous Grillo's strain-channelling equation. Such diffuse scattering covers moderate angles (MAADF and HAADF regimes), and we expect that its contribution should nevertheless disappear in the HAADF regime with very large collection angle, as evidenced by experimental images.

When simulating ADF dislocation images using Grillo's strain-channelling equation, the resulting contrast is highly dependent on diffusion-related parameters as well as on the contribution of Huang scattering. This elastic model, in fact, aims at a description of the effects that a defect and consequently its strain field have on the electron channelling inside the crystal; by means of qualitative parameters (see appendix for a complete description) it allows for the interpretation of the image contrast. In this respect, the sensible parameters are adjusted to better match the experimental images allowing for their interpretation and validation of the model itself. Simulated contrast features in the three regimes show a good agreement with the experimental images, as demonstrated in Fig. 8. The *I-type* contrast however appears slightly wider in the experimental images. This is because the scattered electrons can undergo thermal re-scattering as they propagate into the crystal.

To further study the depth-dependent ADF contrast behaviour, LAADF, MAADF, and HAADF profiles for a dislocation placed at different depths are computed as shown in Fig. 9. The LAADF profiles do not exhibit any remarkable changes as a function of dislocation depth. In the MAADF regime, the profile changes from *I-type* to *M-type* as the dislocation depth is increased; i.e. from an enhanced signal at the core to symmetrical peaks on either side of the dislocation core. This is consistent with experimental observations, further validating the proposed theory based on the attenuation of the *1s* state channelling in the foil depth. Similarly, in the HAADF regime the contrast from the dislocation gradually decreases upon increasing its depth within the foil; a bottom-configuration dislocation is barely visible in this regime. Overall, the close agreement between the experimental and computational images corroborates the proposed model for interpreting the dependence of ADF contrast on dislocation depth and detector collection range.

4. Conclusions

In summary, ADF-STEM image contrast from dislocations in a GaN membrane was systematically studied. Experimental images showed that contrast features are sensitive to the collection range of the ADF detector as well as to the specific depth of the dislocation in the specimen. For a dislocation located close to the entrant foil surface, strain-

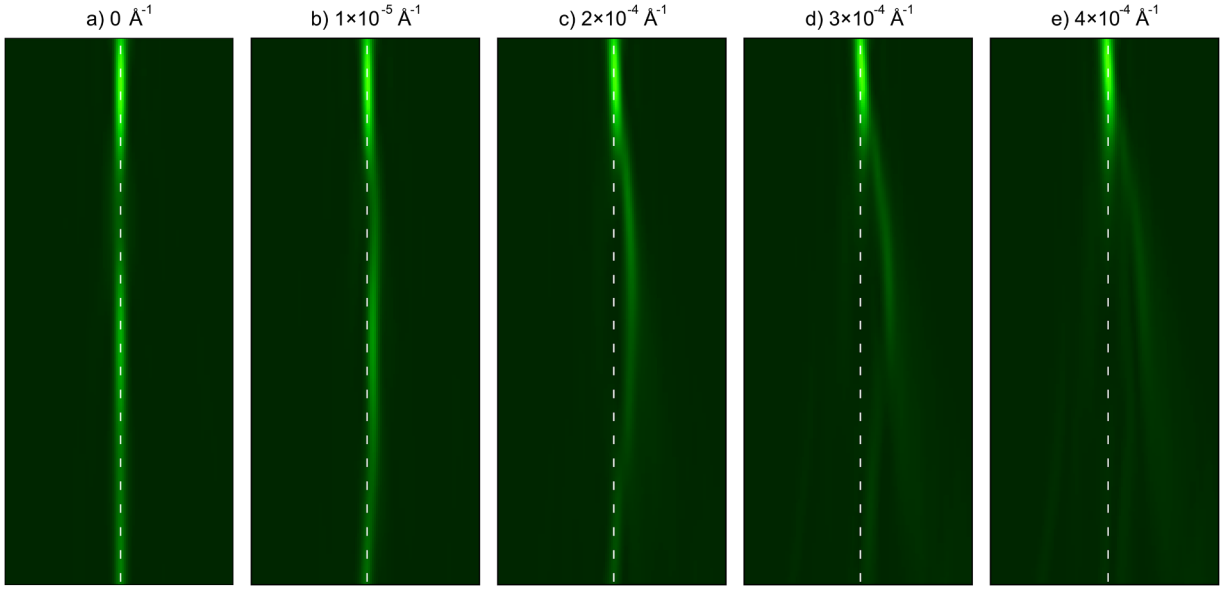

Fig. 7. Multislice simulations showing the effect of atomic column curvature on the electron beam propagation along a 15 nm thick GaN atomic column. The nominal atomic column curvatures are (a) 0 $Å^{-1}$, (b) 1×10^{-5} $Å^{-1}$, (c) 2×10^{-4} $Å^{-1}$, (d) 3×10^{-4} $Å^{-1}$, (e) 4×10^{-4} $Å^{-1}$. Dashed lines represent the intact atomic column.

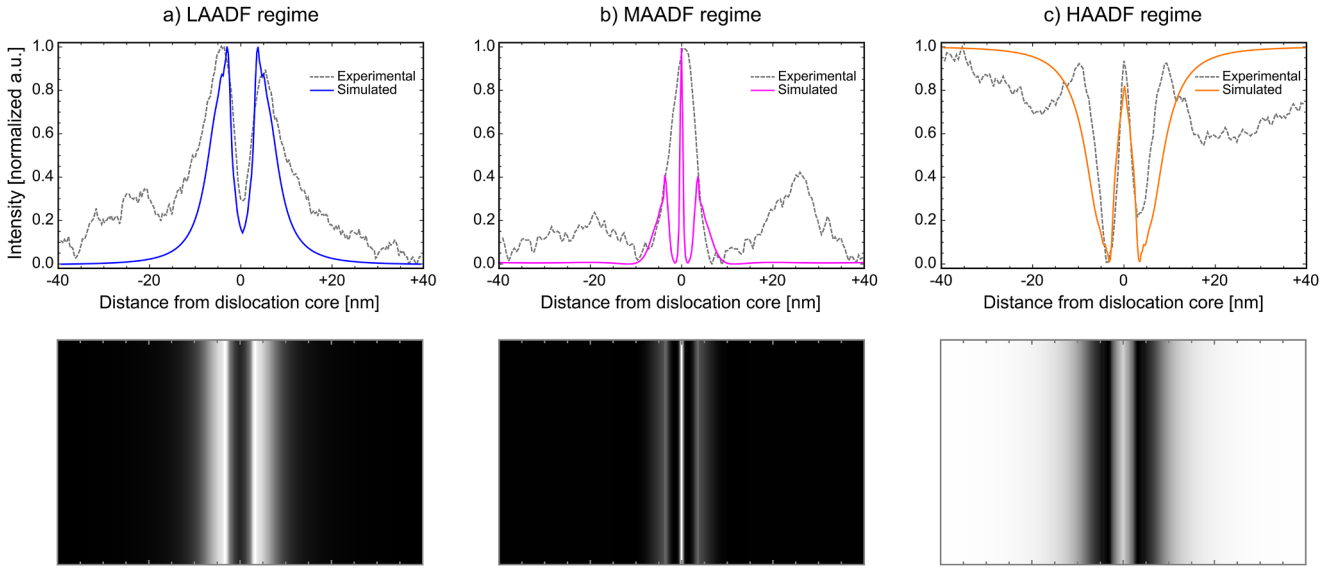

Fig. 8. Comparison between the experimental and simulated ADF-STEM images of a top-configuration dislocation. The top row shows the intensity profiles across the experimental and simulated images for different ADF regimes: (a) LAADF regime, *M-type* contrast; (b) MAADF regime, *I-type* contrast; and (c) HAADF regime, *W-type* contrast. Simulated images are presented in the bottom row.

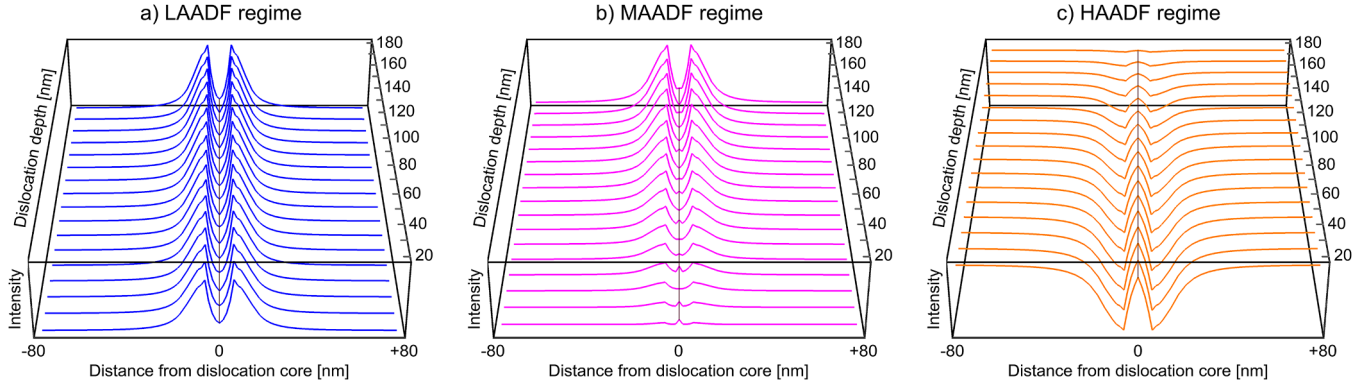

Fig. 9. Evolution of the ADF-STEM dislocation contrast as a function of dislocation depth in the specimen. Intensity profiles across the simulated images from edge-character dislocations of different specific depths in the foil are plotted for all three ADF regimes: (a) LAADF regime, (b) MAADF regime, and (c) HAADF regime.

induced Huang scattering, along with other mechanisms such as de-channelling and redistribution of the Bloch-state population by dislocation, cause signals to be scattered at different angles. Therefore, depending on the ADF detector collection range different contrasts are obtained: the *M-, I-*, and *W-type* contrasts in the LAADF, MAADF, and HAADF regimes, respectively. All the *s*-state related mechanisms, which are believed to be the origin of a positive contrast from the dislocation core in the MAADF and HAADF images, peter out with the distance into the crystal depth, thus the *I-* and *W-type* contrasts are not observed for dislocations that are situated beyond a certain depth. A rationale based on the electron channelling and Bloch-wave scattering was proposed to account for the mechanisms underlying the experimental contrast features. Grillo's strain-channelling equation was implemented for the simulations of the ADF-STEM dislocation contrast to provide a computational validation of the proposed mechanism.

Acknowledgments

E.O. would like to acknowledge: Prof. Pierre Stadelmann, Dr. Duncan T.L Alexander, Dr. Quentin Jeangros of CIME-EPFL, Prof. Peter Nellist of University of Oxford, and Prof. Michael Mills of The Ohio State University for fruitful discussions; Prof. Nicolas Grandjean of LASPE-EPFL for supplying the specimen; Danièle Laub of CIME-EPFL for providing help with TEM sample preparation. Swiss National Science Foundation financially supported this work (project no. 200020-143217). E.R. acknowledges the support from Q-SORT, a project funded by the European Union's Horizon 2020 Research and Innovation Program under grant agreement No. 766970.

Supplementary materials

Supplementary material associated with this article can be found, in the online version, at doi:10.1016/j.ultramic.2019.02.004.

Appendix

This upgraded model directly ties to the classic simple model for the Huang scattering where an additional static Debye-Waller factor M' is added to the normal thermal factor M [40]. This effect can be added to the cross section σ that is:

$$\Delta\sigma \propto \int_{\theta\,\min}^{\theta\,\max} f^2(\theta)\left[1 - e^{-2(M+M')(\theta^2/\lambda^2)}\right]d^2\theta - \int_{\theta\,\min}^{\theta\,\max} f^2(\theta)\left[1 - e^{-2M(\theta^2/\lambda^2)}\right]d^2\theta,$$

where f is the elastic scattering factor, θ is the scattering angle, λ is the electron beam wavelength, M is the Debye-Waller factor and M' is the additional Debye-Waller factor that takes into account the effect of disorder. The additional Debye-Waller factor produces a more rapid absorption of the *1s* state but is not considered herein. Taking into account the factors introduced above, the previously introduced Grillo's set of strain-channelling equations can be written as:

$$\begin{cases} \dfrac{d^2\Phi(x,y,z)}{dz^2} = \left[-2(\mu_{1s} + \mu_{SD})\dfrac{d\Phi_{1s}(x,y,z)}{dz} - 2\left(\dfrac{\Gamma'}{\sigma_\theta}\right)^2\Phi_{1s}(x,y,z)\right] \\ \dfrac{dI_{Huang}(x,y,z)}{dz} = 2H\left(\dfrac{\Gamma'}{\sigma_\theta}\right)^2\Phi_{1s}(x,y,z) \\ I = \int(\Phi_{1s} + C)\left[\sum_{i=atoms}\left(\sigma_i + H'\left(\dfrac{\Gamma''}{\sigma'_\theta}\right)^2\right)\delta(z - z_i)\right]dz + I_{Huang} \end{cases},$$

where Φ_{1s} is the excitation of the *1s*-type Bloch-state, (x,y,z) are the space directions, μ_{1s} is the absorption coefficient of the *1s* Bloch-state, μ_{SD} is the absorption coefficient related to the static displacement, σ_i is the scattering cross section for the i_{th} atom in the relevant atomic column, σ_θ is the size of the *1s* state in the reciprocal space, I_{Huang} is the contribution of Huang scattering, C is an adjustable parameter to account for the contribution of the non-*1s* Bloch-states, and I is the ADF intensity. H' is the parameter that takes into account the extra Huang scattering, and $\Gamma'' = \Gamma - \Gamma'$ is the excess curvature, namely the difference between the real atomic column curvature (Γ) and the maximum curvature that the primary beam is able to follow (Γ').

References

[1] S. Amelinckx, The characterization of defects in crystals, J. Cryst. Growth 24–25 (1974) 6–10.
[2] E. Oveisi, A. Letouzey, D.T.L. Alexander, Q. Jeangros, R. Schäublin, G. Lucas, P. Fua, C. Hébert, Tilt-less 3-D electron imaging and reconstruction of complex curvilinear structures, Sci. Rep. 7 (2017) 10630.
[3] E. Oveisi, A. Letouzey, S. De Zanet, G. Lucas, M. Cantoni, P. Fua, C. Hébert, Stereo-vision three-dimensional reconstruction of curvilinear structures imaged with a TEM, Ultramicroscopy 184 (2018) 116–124.
[4] L. Agudo Jácome, G. Eggeler, A. Dlouhý, Advanced scanning transmission stereo electron microscopy of structural and functional engineering materials, Ultramicroscopy 122 (2012) 48–59.
[5] J. Liu, Scanning transmission electron microscopy and its application to the study of nanoparticles and nanoparticle systems, J. Electron Microsc 54 (2005) 251–278.
[6] J. Zimmermann, H. Van Swygenhoven, C. Marichal, S. Van Petegem, C. Borca, B. Bartova, E. Oveisi, C. Hebert, Slip in directionally solidified Mo-alloy micropillars – part I: nominally dislocation-free pillars, Acta Mater. 60 (2012) 4604–4613.
[7] P. Ercius, D.A. Muller, Incoherent bright field STEM for imaging and tomography of ultra-thick TEM cross-sections, Microsc. Microanal. 15 (2009) 238–239.
[8] P.J. Phillips, M. De Graef, L. Kovarik, A. Agrawal, W. Windl, M.J. Mills, Atomic-resolution defect contrast in low angle annular dark-field STEM, Ultramicroscopy 116 (2012) 47–55.
[9] P.J. Phillips, M.J. Mills, Fine-scale structure of dislocations and debris in deformed Ni-based superalloy R104, Philos. Mag. 93 (2013) 82–95.
[10] D.D. Perovic, C.J. Rossouw, A. Howie, Imaging elastic strains in high-angle annular dark field scanning transmission electron microscopy, Ultramicroscopy 52 (1993) 353–359.
[11] J.M. Cowley, M.S. Hansen, S.Y. Wang, Imaging modes with an annular detector in STEM, Ultramicroscopy 58 (1995) 18–24.
[12] S. Hillyard, J. Silcox, Detector geometry, thermal diffuse scattering and strain effects in ADF STEM imaging, Ultramicroscopy 58 (1995) 6–17.
[13] T. Walther, Y. Qiu, A.G. Cullis, Measuring the contrast in annular dark field STEM images as a function of camera length, J. Phys. Conf. Ser. (2010) 241.
[14] J.M. Cowley, Y. Huang, De-channelling contrast in annular dark-field STEM, Ultramicroscopy 40 (1992) 171–180.
[15] D.M. Maher, D.C. Joy, The formation and interpretation of defect images from crystalline materials in a scanning transmission electron microscope, Ultramicroscopy 1 (1976) 239–253.
[16] V. Grillo, F. Rossi, A new insight on crystalline strain and defect features by STEM–ADF imaging, J. Cryst. Growth 318 (2011) 1151–1156.
[17] V. Grillo, K. Mueller, K. Volz, F. Glas, T. Grieb, A. Rosenauer, Strain, composition and disorder in ADF imaging of semiconductors, J. Phys. Conf. Ser. 326 (2011) Article number 012006.
[18] D.D. Perovic, A. Howie, C.J. Rossouw, On the image contrast from dislocations in

high-angle annular dark-field scanning transmission electron microscopy, Philos. Mag. Lett. 67 (1993) 261–272.
[19] P.J. Phillips, M.C. Brandes, M.J. Mills, M. de Graef, Diffraction contrast STEM of dislocations: imaging and simulations, Ultramicroscopy 111 (2011) 1483–1487.
[20] P.J. Phillips, M.J. Mills, M. De Graef, Systematic row and zone axis STEM defect image simulations, Philos. Mag. 91 (2011) 2081–2101.
[21] B.G. Mendis, K.J. Hemker, Bloch wave analysis of the Eshelby twist contrast around end-on screw dislocations in BCC Mo, Ultramicroscopy 108 (2008) 855–864.
[22] S.J. Pennycook, D.E. Jesson, High-resolution incoherent imaging of crystals, Phys. Rev. Lett. 64 (1990) 938–941.
[23] S.J. Pennycook, D.E. Jesson, High-resolution Z-contrast imaging of crystals, Ultramicroscopy 37 (1991) 14–38.
[24] P.D. Nellist, S.J. Pennycook, The principles and interpretation of annular dark-field Z-contrast imaging, in: W.H. Peter (Ed.), Advances in Imaging and Electron Physics, Elsevier, 2000, pp. 147–203.
[25] S.J. Pennycook, Z-contrast STEM for materials science, Ultramicroscopy 30 (1989) 58–69.
[26] P.D. Nellist, S.J. Pennycook, Incoherent imaging using dynamically scattered coherent electrons, Ultramicroscopy 78 (1999) 111–124.
[27] K. Huang, X-ray reflexions from dilute solid solutions, Proc. R. Soc. London Ser. A. Math. Phys. Sci. 190 (1947) 102–117.
[28] Z. Wang, Dynamical theories of dark-field imaging using diffusely scattered electrons in STEM and TEM, Acta Crystallographica Section A 51 (1995) 569–585.
[29] Z.L. Wang, Dislocation contrast in high-angle hollow-cone dark-field TEM, Ultramicroscopy 53 (1994) 73–90.
[30] Z.L. Wang, Elastic and Inelastic Scattering in Electron Diffraction and Imaging, Plenum Press, New York, 1995.
[31] V. Grillo, E. Carlino, F. Glas, Influence of the static atomic displacement on atomic resolution Z-contrast imaging, Phys. Rev. B 77 (2008) 054103.
[32] V. Grillo, The effect of surface strain relaxation on HAADF imaging, Ultramicroscopy 109 (2009) 1453–1464.
[33] V. Grillo, E. Rotunno, STEM_CELL: a software tool for electron microscopy: part I—simulations, Ultramicroscopy 125 (2013) 97–111.
[34] L. Lugani, J.F. Carlin, M.A. Py, D. Martin, F. Rossi, G. Salviati, P. Herfurth, E. Kohn, J. Bläsing, A. Krost, N. Grandjean, Ultrathin In AlN/GaN heterostructures on sapphire for high on/off current ratio high electron mobility transistors, J. Appl. Phys. 113 (2013) 214503.
[35] D.B. Williams, C.B. Carter, Transmission electron microscopy: a textbook for materials science, 2009.
[36] V. Grillo, F. Rossi, STEM_CELL: a software tool for electron microscopy. Part 2 analysis of crystalline materials, Ultramicroscopy 125 (2013) 112–129.
[37] E. Oveisi, Three-dimensional STEM imaging of dislocations (Ph.D. thesis), Faculty of basic sciences, EPFL, 2015.
[38] B. Schaffer, W. Grogger, G. Kothleitner, Automated spatial drift correction for EFTEM image series, Ultramicroscopy 102 (2004) 27–36.
[39] A. Howie, M.J. Whelan, Diffraction contrast of electron microscope images of crystal lattice defects. III. Results and experimental confirmation of the dynamical theory of dislocation image contrast, Proc. R. Soc. London, 1962, pp. 206–230.
[40] Z. Yu, D.A. Muller, J. Silcox, Study of strain fields at a-Si/c-Si interface, J. Appl. Phys. 95 (2004) 3362–3371.